PAPER • OPEN ACCESS

Direct visualization of nanoparticle morphology in thermally sintered nanoparticle ink traces and the relationship among nanoparticle morphology, incomplete polymer removal, and trace conductivity

To cite this article: Ghansham Rajendrasingh Chandel *et al* 2023 *Nanotechnology* **34** 365705

OPEN ACCESS
IOP Publishing
Nanotechnology

Nanotechnology **34** (2023) 365705 (14pp)
https://doi.org/10.1088/1361-6528/acd9d2

Direct visualization of nanoparticle morphology in thermally sintered nanoparticle ink traces and the relationship among nanoparticle morphology, incomplete polymer removal, and trace conductivity

Ghansham Rajendrasingh Chandel[1,5], Jiayue Sun[2,5], Sai Ankit Etha[1], Beihan Zhao[1], Vishal Sankar Sivasankar[1], Shakiba Nikfarjam[3], Mei Wang[3], Daniel R Hines[4], Abhijit Dasgupta[1], Taylor Woehl[3] and Siddhartha Das[1]

[1] Department of Mechanical Engineering, University of Maryland, College Park, MD 20742, United States of America
[2] Department of Chemistry and Biochemistry, University of Maryland, College Park, MD 20742, United States of America
[3] Department of Chemical and Biomolecular Engineering, University of Maryland, College Park, MD 20742, United States of America
[4] Laboratory for Physical Sciences, 8050 Greenmead Drive, College Park, MD 20740, United States of America

E-mail: sidd@umd.edu

Received 1 November 2022, revised 18 April 2023
Accepted for publication 30 May 2023
Published 19 June 2023

Abstract

A key challenge encountered by printed electronics is that the conductivity of sintered metal nanoparticle (NP) traces is always several times smaller than the bulk metal conductivity. Identifying the relative roles of the voids and the residual polymers on NP surfaces in sintered NP traces, in determining such reduced conductivity, is essential. In this paper, we employ a combination of electron microscopy imaging and detailed simulations to quantify the relative roles of such voids and residual polymers in the conductivity of sintered traces of a commercial (Novacentrix) silver nanoparticle-based ink. High resolution transmission electron microscopy imaging revealed details of the morphology of the inks before and after being sintered at 150 °C. Prior to sintering, NPs were randomly close packed into aggregates with nanometer thick polymer layers in the interstices. The 2D porosity in the aggregates prior to sintering was near 20%. After heating at 150 °C, NPs sintered together into dense aggregates (nanoaggregates or NAgs) with sizes ranging from 100 to 500 nm and the 2D porosity decreased to near 10%. Within the NAgs, the NPs were mostly connected via sintered metal bridges, while the outer surfaces of the NAgs were coated with a nanometer thick layer of polymer. Motivated by these experimental results, we developed a computational model for calculating the effective conductivity of the ink deposit

[5] Contributed equally.

represented by a prototypical NAg consisting of NPs connected by metallic bonds and having a polymer layer on its outer surface placed in a surrounding medium. The calculations reveal that a NAg that is 35%–40% covered by a nanometer thick polymeric layer has a similar conductivity compared to prior experimental measurements. The findings also demonstrate that the conductivity is less influenced by the polymer layer thickness or the absolute value of the NAg dimensions. Most importantly, we are able to infer that the reduced value of the conductivity of the sintered traces is less dependent on the void fraction and is primarily attributed to the incomplete removal of the polymeric material even after sintering.

Supplementary material for this article is available online

Keywords: nanoparticles, morphology, sintering, trace conductivity

(Some figures may appear in colour only in the online journal)

1. Introduction

The use of metal nanoparticle (NP) inks has been central in the additive manufacturing of printed electronics [1–3]. NP inks generally consist of highly concentrated (>30 wt%) colloidal metal NPs in a low vapor pressure solvent, such as water. The NPs are passivated with a polymer layer that gives them colloidal stability before and during ink printing, preventing formation of large heterogeneous NP aggregates in the ink. After printing, the NP ink trace is heated to remove the solvent and the polymeric stabilizer, and to aggregate and sinter the NPs into a monolithic trace [1–3]. Heating causes sintering of the NPs and increased conductivity of the NP traces. It has been suggested that increasing the heat treatment temperature and time leads to more efficient NP aggregation and sintering and a larger conductivity of the NP traces (i.e. closer to the conductivity of the corresponding bulk metals). For example, sintering silver NPs at 140 °C for 10–15 min resulted in a conductivity of the sintered traces that is ∼30% of the bulk silver conductivity [4, 5]. On the other hand, sintering silver NPs for 10 min at 60 °C produced a conductivity of the sintered traces that was only 10%–12% of the bulk silver conductivity [5]. In addition to simple heating, other methods of sintering have also been employed resulting in typically reduced conductivities as compared to what is accomplished by simple heating. For example, room-temperature chemical sintering leads to sintered traces with conductivities that were 15%-20% of the bulk silver [6, 7]. Under such circumstances the simple heating based sintering procedure still remains the most practiced method for sintering of printed metal NP (especially silver NP) traces.

What fundamental physico-chemical processes occur when the printed NP ink traces are subjected to simple heating-based sintering? This has been one an important question that needs to be answered for developing a more widely usable NP based ink for printed electronics applications. The current hypothesis is that sintering leads to the following processes: (1) evaporation of the solvent causes the NPs to come very close to one another through capillary forces; (2) the polymer capping ligands on the NP surface is removed from the NP surface; and (3) the NPs aggregate and sinter to form metallic contacts. Sintering occurs due to the thermodynamic driving force that reduces the amount of surface area and regions of high curvature between particles, with the elevated temperature leading to enhanced surface diffusion of silver towards the region of high curvature. In order to confirm this hypothesis, it is necessary to quantify the structure of the sintered traces at a resolution that allows the visualization of not only the individual NPs, as has been achieved using scanning electron microscopy (SEM) imaging of NP aggregates/agglomerates within the sintered inks [8–17], but also the NP-capping polymeric coating. Unfortunately, such visualization inside an ink trace before and after sintering has not yet been achieved. State-of-the-art transmission electron microscopy (TEM) imaging experiments have delineated NPs (or NP clusters) in a sintered trace, but these images did not visualize the polymer capping ligand or the NP–NP inter-metallic necking [14, 18–20]. A lack of well-resolved visualization of both polymer layers and metal NPs inside a fully sintered ink, therefore, has limited the current understanding of the physico-chemical processes involved in the sintering of metallic NP ink to speculation.

In this paper, we employ a combination of nanoscale visualization experiments with TEM and SEM and detailed computations to unravel the key physics dictating the conductivity of sintered silver NP traces. First, we image at nanometer scale resolution the configuration and the morphology of the silver NPs (and the nano-aggregates or NAgs that they constitute) and the thickness and location of polymer capping layers in an ink deposit before and after drying/sintering (either dried at room temperature or sintered at 150 °C). For the ink dried at room temperature, we identify distinct polymeric capping ligand layers, which separate aggregated NPs. For the ink traces sintered at 150 °C, we find a large number of NPs sinter and aggregate forming NAgs or self-assembled NAgs, where there exist distinct inter-metallic necks between neighboring NPs. This suggests a pronounced onset of direct NP–NP metallic contacts that will lead to a larger trace conductivity. *On the other hand, while the thickness of the existing polymer coating (on the NAgs) reduces after sintering at an elevated temperature, they do not completely disappear.* This particular configuration trace enables us to identify that the conductivity of the traces is a combination of the bulk metallic conductivity that is associated with the direct NP–NP contacts or necking and tunneling conductivity that is associated with indirect contact between the NPs or NP aggregates *through an*

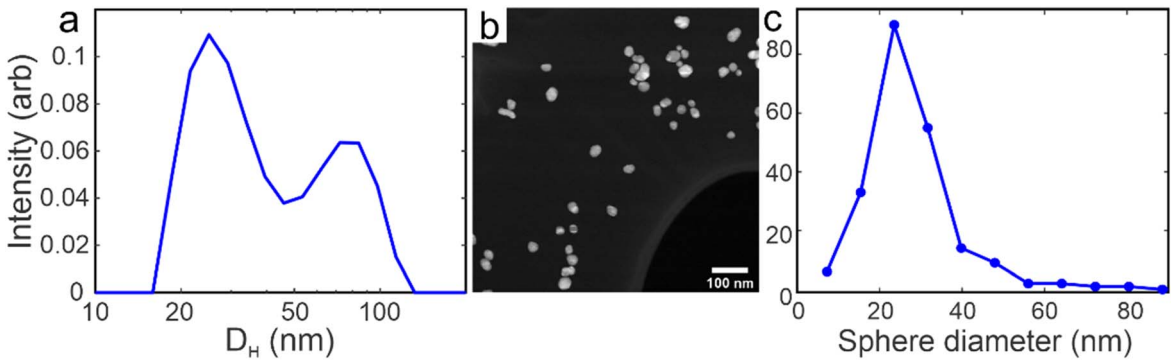

Figure 1. Particle size analysis of silver NPs. (a) Dynamic light scattering distribution of silver NP ink after diluting 18 000 times by volume. (b) Representative dark field STEM image of silver NPs from the ink dispersion. (c) Particle size distribution of the NPs determined by particle counting of STEM images such as that shown in (b). Data shows the equivalent sphere diameter of the particles as determined from STEM.

intervening low conductivity organic layer. We justify such a consideration by noting that the experimentally observed conductivity of thermally sintered traces is ∼30% of the bulk silver conductivity, even when factoring in the effect of appropriate porosity for the sintered traces [21]. These observations beg the question: *What is the conductivity of the sintered traces consisting of NPs and NAgs that are partially covered by an interstitial polymeric material?* Answering this question, therefore, is the next important step of this study. For this purpose, we employ COMSOL based simulations for calculating the effective conductivity of a system consisting of a NP aggregate, with metal–metal NP contact within, that is partly covered by a polymeric interphase material and surrounded by a region of reduced conductivity. Existing simulation studies in the literature probing the conductivity of sintered NP aggregates do not consider the effect of the presence of such residual polymeric interphase layer [22, 23]. Quantification of the average conductivity from the simulation results reveals that 35%–40% polymer coverage on the NP surface area leads to a trace conductivity equivalent to previous experiments (30% of bulk conductivity) [4, 5]. We also simulate a more realistic case, where instead of a single NAg, we consider a structure consisting of self-assembled NAg: for such a structure, the percentage of polymer coverage necessary to ensure a trace conductivity that is 30% of the bulk conductivity is slightly more than that for the case of a single NAg. In all these calculations, we account for the effect of voids that are present (and measured separately) in the sintered traces, and we find that these voids have a much lesser influence in reducing the conductivity of the sintered traces as compared to the presence of the residual polymer layer present on the NP surface even after the sintering. In fact our finding is in line with a recent experimental study that has identified the significance of the presence of residual polymeric layer, post low-temperature sintering or sintering at 100 °C–200 °C, in significantly reducing the overall conductivity of the metal NP deposits [24]. Previous studies have pointed to the continuous increase in the conductivity of the silver NP traces with an increase in the sintering temperature: however, none of these studies identify or quantify the extent of the existence of the polymer coating on the surface of the individual NPs or individual NAgs even at the sintering temperatures and the manner in which the existence of such residual polymer coating (even after sintering) leads to the reduced conductivity of the sintered traces [25–27].

2. Results

2.1. Experimental results on the morphology of the nanoparticles inside the sintered traces

The purpose of this section is to quantify our experimental findings pinpointing the morphology of the NPs inside the sintered traces: specifically, we are interested to identify (a) the average size of the NP aggregates; (b) the (possible) presence of polymeric/organic coating around the individual NPs or NP aggregates; (c) the average thickness of such polymeric/organic coating; (d) the average porosity of the NP aggregates.

The silver NP ink particle properties and ink deposits were characterized using dynamic light scattering (DLS) and TEM to provide input parameters for the conductivity model. The NPs were dispersed at 40 wt% in diethylene glycol and water. Due to the high particle concentration in the ink, it was diluted ∼18 000 times by volume with water for the DLS analysis and 1000 times by volume for TEM analysis of the particle size distribution (PSD). DLS gives a qualitative measure of the PSD based on the particles' hydrodynamic diameter, while the TEM imaging and image analysis generate a quantitative PSD based on particle counting approaches. Figure 1(a) shows the DLS PSD based on scattering intensity, which shows peaks centered at ∼25 and ∼80 nm. In the intensity-based PSD distribution, even relatively small concentrations of large particles give a substantial peak height due to their large scattering intensity, where scattering intensity scales with radius to the sixth power. Therefore, we attribute the 25 nm peak to unaggregated particles, which make up the majority of particles in solution, while the 80 nm peak represented a minority fraction of aggregated particles. Dark field scanning TEM (STEM) imaging was used to determine the PSD of the NPs in the diluted ink (figure 1(b)). The NP shapes (figure 1(c)) ranged from spherical to oblong and had sizes ranging from about 10–60 nm with the majority of particles near 20 nm in diameter, consistent with the DLS

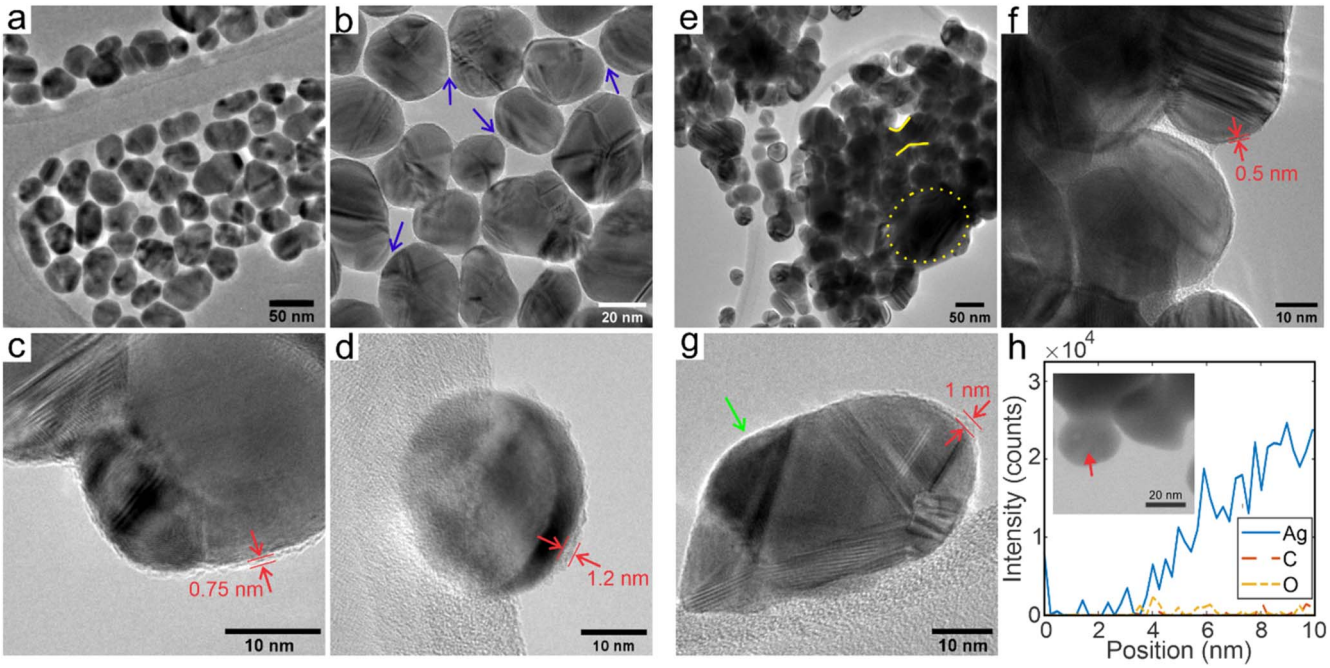

Figure 2. TEM imaging and elemental analysis of dried NP deposits and surface organic coating before (a)–(d) and after (e)–(h) sintering at 150 °C for 15 min. (a) Low magnification TEM image of unsintered silver NP deposit (dried at room temperature) formed by drop casting the ink diluted 10 times in water. (b) Image showing interparticle connections separated by a thin organic layer (blue arrows). (c)–(d) High magnification TEM images showing ∼1 nm uniform amorphous organic layer coating the surface of each silver NP. (e) TEM image of sintered NP deposits showing NPs form metallic necks and 100–500 nm sintered aggregates. The solid yellow lines highlight a region where a neck was observed to form between two sintered neighboring NPs while the dashed yellow circle highlights a large grain that has formed by complete sintering. (f)–(g) High magnification TEM images show the organic coating layer is non-uniform after sintering and coats the outside of the sintered aggregates. Green arrow in (g) shows an example of a particle surface with patchy surface organic coating. (h) Energy dispersive x-ray spectrometry (EDS) elemental analysis line scan at the surface of a sintered silver NP showing the absence of surface oxidation. The red line indicates the line across which EDS signal was acquired.

measurements. There were a few particle aggregates observed with TEM with sizes >40 nm, again consistent with DLS; however, because the TEM PSD is on a particle number basis, the PSD appears monomodal (figure 1(c)).

To simulate the ink printing process, microliter volumes of the NP ink, diluted 10 times by volume, were drop cast onto thin, porous carbon networks on TEM grids. It was necessary to dilute the nanoparticle ink by 10 times prior to deposition because the fully concentrated ink formed thick 3D deposits that could not be imaged with TEM. The goal of the imaging experiments was not to take images of a realistic ink deposit but instead to determine how sintering affected the polymer coating layer on the nanoparticles and to provide experimental measurements of polymer layer thickness and coverage as inputs for the numerical conductivity model. We selected regions of the TEM sample that had close packed silver nanoparticles in 2D film configurations, which most closely replicated the close-packed arrangement of nanoparticles in a real ink deposit and facilitated measuring the approximate polymer coating thickness and coverage after sintering. Thermogravimetric analysis (TGA) showed that baking to 150 °C resulted in a ∼64% reduction in the mass of the ink deposit (see figure S2 in the supplementary material), due primarily to evaporation of residual solvent.

Low magnification TEM images of the unsintered sample (dried in air) showed that close-packed 2D NP aggregates formed over some of the holes in the lacey carbon network with high NP loading (see figure 2(a)). Higher resolution TEM images taken under defocused conditions revealed that interparticle contacts in the deposit had amorphous conformal ∼1 nm organic films in between (see figure 2(b), blue arrows). There were no metallic connections between neighboring particles. Each NP was surrounded by a conformal (∼1 nm) amorphous organic film (see figures 2(c), (d), red arrows), which is likely a polymeric or organic molecule capping ligand layer that stabilizes particles in the ink dispersion and prevents aggregation. Here, we define a conformal coating as one that allowed no exposure of bare nanoparticle surface, but could have some roughness and nonuniform thickness. In some cases, the organic coating layer was non-uniform and showed local variations in thickness ranging from 0.5 to 1.5 nm. While the TEM images do not reveal the composition of these films, the image contrast is consistent with an amorphous organic, potentially polymeric, film [28]. Figures 2(e)–(g) show the TEM images of the NP deposits after being sintered directly on the carbon TEM sample at 150 °C for 15 min in air. Significant interparticle sintering with metallic necks forming between particles was observed in regions of high NP concentration (figure 2(e)). Sintered NP aggregates (caused by the sintering-driven aggregation of the NPs) formed with sizes on the order of 100–500nm. Closer interrogation showed that within the aggregates the NPs were almost exclusively attached by metallic contacts, but that some particles retained thin organic layers on their surface (see

figures 2(f),(g)). Likewise, the outside of the aggregates was coated by a thin organic layer. Nearly all organic coating layers were non-conformal or patchy after sintering, indicating removal of some of the organic layers. A non-conformal coating was defined as one with both surface roughness and bare regions of the nanoparticle with no observed amorphous layer. The retention of the organic capping layer was not surprising given the low sintering temperature of 150 °C, which is well below the decomposition temperature of common polymers used as capping ligands (for example, polyvinylpyrollidone and dodecanethiol on NPs start to decompose at 350 °C) [29, 30]. We have also conducted sintering at 300 °C and found that all the polymer was removed (see figure S1 in the supporting information). For the present case (i.e. traces sintered at 150 °C), elemental analysis of the surface of a sintered NP with energy dispersive x-ray spectrometry (EDS) showed that there was no oxygen, indicating no surface oxidation occurred during sintering (see figure 2(h)). No carbon signal was detected with the EDS, likely because the amount of carbon was below the detection limit of EDS (∼0.1 wt%), but the high-resolution TEM images of the layer are consistent with the morphology of a thin amorphous layer of organic molecules, such as a polymer.

We prepared thin layers of NP deposits on a thin carbon TEM sample film and performed image analysis and statistical analysis to assess the porosity of the as-made and sintered NP deposits. Image analysis was used to compute the area fraction of the NP material in NP deposits for more than ten 100 nm × 100 nm regions in several different low magnification TEM images of the as-made and sintered samples (see figures 3(a), (b), orange boxes). The regions were selected randomly from different regions of each sample. The particle area fraction was calculated for each region by dividing the total area occupied by NPs by the total area of the sample region (100^2 nm^2). The pore area fraction is obtained by subtracting the particle area fraction from one. Figure 3(c) shows box plots of the porosity fraction for each sample, where the NP deposits had a median pore fraction of 0.18 in the unsintered sample and 0.12 in the sintered sample. Statistical analysis using a Wilcoxon rank sum test showed that the median pore fractions were significantly different from each other with a p-value of $p = 0.0014$. These measurements demonstrate that sintering leads to both the formation of metallic interparticle necking as well as densification of the NP deposits through the reduction of porosity.

Factors such as the local initial pore fraction, nanoparticle size distribution, polymer coating thicknesses, and other kinetic factors can affect the local amount of sintering and the final pore fraction. Before and after TEM images of the nanoparticle deposits were not taken at the same exact sample locations, so it is not possible to rationalize the final pore fraction in terms of these factors. Instead, the goal of this measurement was to provide experimental inputs for pore fraction of the sintered nanoparticle deposit into the numerical conductivity model.

2.1.1. Summary of the experimental findings. The experiments unravel two key issues. First and foremost, it established that there is polymeric surface coverage on the metal nanoparticle nano-aggregates even after sintering at 150 °C. Second, it provided an estimation of the pore fraction in the sintered traces, which could be used as input for our simulations. It is important to note that while we are able to identify the presence of the polymeric layer on the sintered metal nanoparticle nano-aggregates, we cannot provide an exact number specifying the extent surface coverage. TEM imaging and TGA measurements cannot accurately measure the residual polymer coating because of the lack of 3D information in TEM images, the wide particle-to-particle variation of polymer coating, and the presence of physisorbed water in the ink deposit that convolutes TGA measurements. As a result, we would need simulations (motivated by the geometric structure revealed by the experiments and the experiment-revealed information of the presence of the polymeric coating even for the sintered nanoaggregates) to quantify the exact extent of the polymeric surface coverage of the nano-aggregates that leads to the observed decreased conductivity of the sintered metal nanoparticle traces. Importantly, as will be revealed below, the numerical simulations are uniquely capable of revealing the amount of residual polymer necessary to achieve experimentally observed conductivity reduction in printed inks.

2.2. Simulation results: quantification of the conductivity of the sintered traces

The experimental TEM imaging provided several key measurements (summarized in table 1) to build a numerical model of NP trace conductivity. Let us first consider the situation where we express the conductivity of the sintered traces simply as the bulk metallic conductivity with the consideration of the appropriate pore fraction. Under such circumstances, following Rosker *et al* [21] we can express the conductivity of the sintered traces as:

$$\sigma_{\text{sin,pore}} = \sigma_m \left[\frac{2(1 - \varphi_{\text{void}})}{2 + \varphi_{\text{void}}} \right], \tag{1}$$

where $\sigma_{\text{sin,pore}}$ is the conductivity of the sintered traces, σ_m is the conductivity of the bulk metal, and φ_{void} is the void fraction (or pore fraction). Using $\varphi_{\text{void}} = 0.12$, we can use equation (1) to obtain:

$$\sigma_{\text{sin,pore}} = 0.83\sigma_m. \tag{2}$$

This is too large a conductivity value for the sintered traces given the fact that experimental study reports a conductivity of the sintered traces of $\sigma_{\text{sin,pore}} = \sigma_{\text{observed}} \sim 0.3\sigma_m$.

2.2.1. Proposed geometry and connection to experimental results. Under such circumstances, we refer to the situation as elucidated by the TEM imaging of the sintered traces (please see figures 2(e)–(g) and the associated discussions) showing that inside the NAgs the NPs were almost exclusively attached by metallic contacts, with the surface of the aggregate coated by a thin, non-uniform polymeric layer. This indicates that some NAgs form direct metal–metal contacts with each other, while others are connected indirectly via an intervening polymeric layer. We shall like to differentiate here between the metallic contacts formed between individual NPs inside a NAg

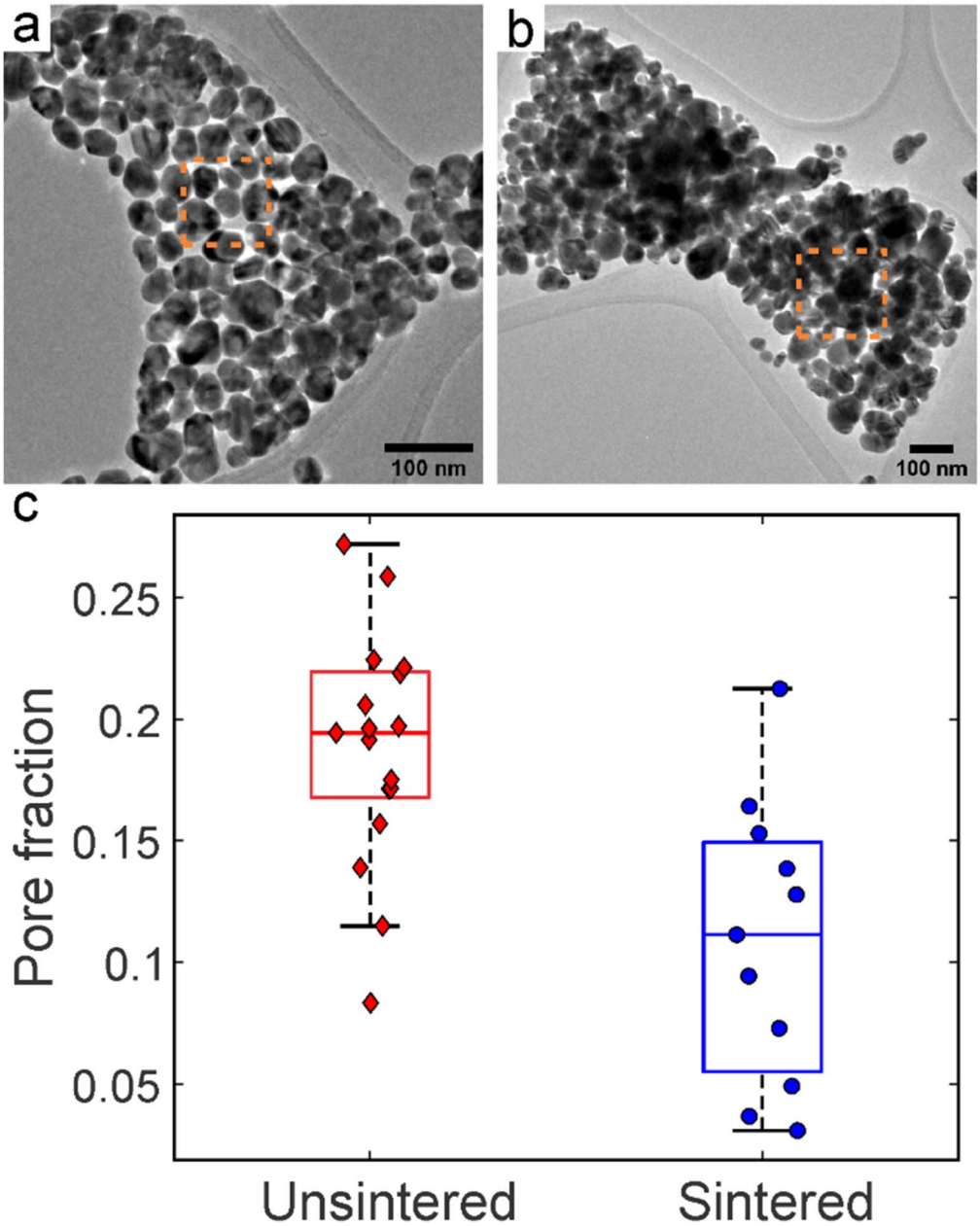

Figure 3. Quantitative analysis of the porosity of the NP deposit. (a), (b) Representative TEM images used to measure the deposit porosity, where (a) is unsintered and (b) is sintered. The orange boxes show example regions where a single porosity measurement was taken. (c) Box plots of pore fraction for unsintered (and dried in air) and sintered NP deposits. The median porosity of the sintered sample was statistically larger than the unsintered sample with a p-value of $p = 0.0014$ as determined by a Wilcoxon rank sum test.

and the contacts formed between two NAgs. Inside a NAg, the individual NPs are primarily forming direct metal–metal contacts; on the other hand, two NAgs can either form a direct metal–metal contact or an indirect contact through an intervening polymeric layer. The simplest way to consider such a system is shown in figure 4, which shows a NAg that is partially covered (on its outer surface) by the polymeric capping layer. The extent of the NAg surface that is covered by this polymeric layer can be made to vary by varying the conical angle α (see figure 4). As this conical angle increases, more and more percentage of the surface area is coated by polymer and will participate in tunneling conduction (*tunneling conduction* [25–27] *becomes important when two NAgs come in contact with each other through the intervening polymeric layer that is present on the surface of one or both of the NAgs*) and a lesser percentage area contributes to direct metal–metal contact (between two NAgs). With such a

Table 1. Summary of the sintered NP aggregate properties determined from TEM.

TEM measured model inputs	
NP aggregate size	100–500 nm
Polymer layer thickness (t_{int})	0.3–1 nm
Aggregate void fraction (φ_{void})	0.12

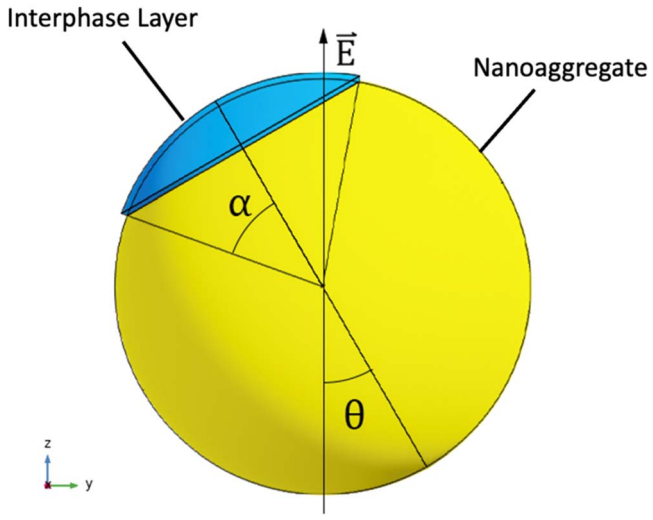

Figure 4. Schematic of a NAg (inside which all the NPs form a direct metal–metal contact) with a layer of interphase polymeric material covering a portion of the outer surface of the NAg. Such a NAg is typically witnessed for the case of sintered (at 150 °C) ink traces. The conical angle 'α' determines the percentage of surface area covered by the interphase polymer, whereas the orientation angle 'θ' accounts for random orientation of the NAgs in the printed traces with respect to the applied electric field '$\vec{E}$'.

geometry, we see that the conductivity is now dependent on the direction of electric field. We expect the minimum conductivity for the case when the cone axis is in line with the electric field, i.e. the case where the electric field is most distorted due to a head-on obstruction from interphase cap. On the other hand, the maximum conductivity is expected when the cone axis is perpendicular to the electric field i.e. when the electric field is mostly parallel to the surface of the interphase cap causing comparatively less disturbance in the electric field. However, in actual inks, the polymer layer may be in any direction relatively, and as a statistical average, we assume each of the angle orientation as equiprobable. Thus, the average conductivity is calculated by averaging over angle (θ).

It is useful to understand the manner in which such simplistic consideration of individual NAgs partially covered by the polymeric material enables reproducing the structure suggested by experiments (see figure 2). To do that, let us consider the three possible cases in which a NAg might exist. These three cases are (1) a NAg that shows no coverage by the polymeric interphase material leading to a self-assembled system of NAgs where the NAgs are only connected via direct metal–metal contacts (this scenario is not encountered for either air-dried ink or sintered ink) (see figure 5(a)); (2) a NAg (inside which all the NPs themselves are connected to each other via the intervening polymeric layer) that shows complete coverage by the polymeric interphase material leading to a system of self-assembled NAgs where the NAgs are always connected to each other by indirect metal–metal contacts through the intervening interphase polymeric material (this scenario is encountered for the case of air-dried ink, as evidenced by the experimental results of figure 2) (see figure 5(b)); (3) a NAg (inside which all the NPs are connected to each other via direct metallic bonds), which is partially covered by an interphase polymeric layer (such a NAg has been pictured in figure 4), which results in a system of self-assembled NAgs with both direct metal–metal contacts and indirect metal–metal contacts separated by a polymer layer (this scenario is encountered for the inks sintered at 150 °C, as evidenced by the experimental results of figure 2) (see figure 5(c)).

2.2.2. Simulation domain and different (constant) conductivity values associated with the different regions constituting this domain. The simulation domain considered in our study has been shown in figure 6. It consists of the representative NAg with a partial surface coverage by the polymeric layer (see figure 4) and the surroundings. We identify three regions in the entire simulation domain: region 1 is the NAg (minus the polymeric layer), region 2 is the polymer-layer part of the NAg, and region 3 is the surroundings. In order to perform the simulations, which in turn will provide the equivalent conductivity, we first need to ascribe uniform average conductivity values to these three regions.

For the polymeric layer depicted as region 2, which leads to the indirect metal–metal contact (through the intervening polymeric layer) between two NAgs, the electrical conductivity is the *tunneling conductivity* (σ_{int}). To calculate the tunneling conductivity, we use the Simmons' formula derived for electron tunneling between two metal surfaces separated by thin insulating film [28–30]. It shows that σ_{int} (see equation (3) below) decreases exponentially with the thickness (t_{int}) of the interphase (insulating film) layer:

$$\sigma_{\text{int}} = \frac{e^2(2m\lambda)^{1/2}}{h^2}\exp\left(\frac{-4\pi(t_{\text{int}})}{h}(2m\lambda)^{\frac{1}{2}}\right). \quad (3)$$

Here, λ is the potential barrier the electron needs to transverse to tunnel, which is close to the work function of metal [31] (which is 4.2 eV for our case). Furthermore, $m = 9.109\,3829 \times 10^{-31}$ kg is the mass and $e = 1.602\,176\,565 \times 10^{-19}$ C is the charge of an electron, and $h = 6.626\,068 \times 10^{-34}$ m^2 kg s^{-1} is the Planck's constant.

Next is the conductivity associated with region 1, which is the metallic part (or polymer-layer-free part) of the NAg: this part leads to the *direct* NAg–NAg contact (without any intervening polymeric layer) and hence must be attributed a uniform bulk metallic conductivity σ_m. Finally, the conductivity associated with the surroundings (i.e. region 3 in figure 6) can be considered as $\sigma_{\text{sin,exp}} = 0.3\sigma_m$.

2.2.3. Governing equations for obtaining the equivalent conductivity. With the knowledge of the different conductivity values associated with the different regions of the simulation domain (see figure 6), the next task that needs to be performed for calculating the equivalent conductivity is to solve for the electric field and the current density, average these quantities in our simulation domain, and derive the average conductivity from their ratio. Classically, several papers have provided closed-form, analytical solutions for the equivalent conductivity of a highly symmetric (e.g. in the form of cylinders or spheres) heterogenous system [28, 29]. On the other hand, the objective of the present study is to quantify the equivalent conductivity for a system represented

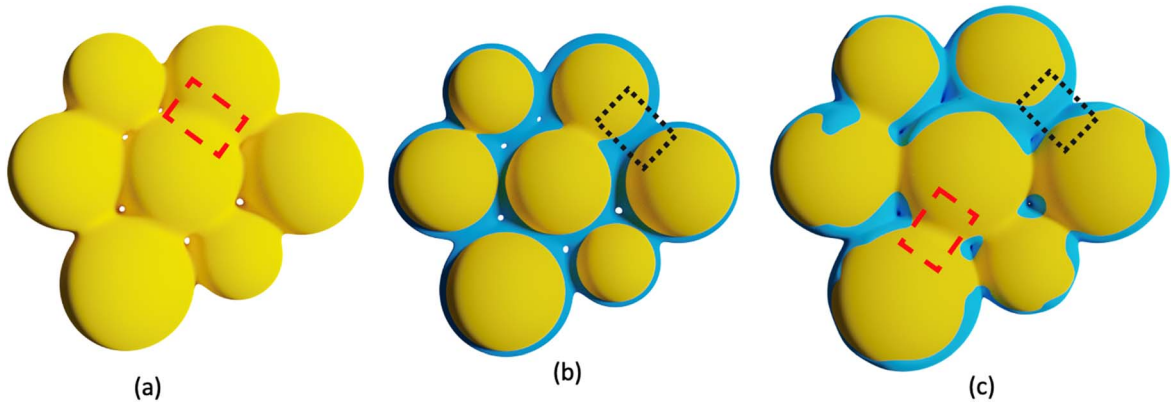

Figure 5. Schematic of the three types of self-assembled system of NAgs constituting the dried/sintered traces. (a) Schematic of a self-assembled system of NAgs where the individual NAgs are connected to one another exclusively through direct metal–metal contacts (see the red dashed box denoting one such contact); no experimental results point to such a scenario. (b) Schematic of a self-assembled system of NAgs where the individual NAgs are connected to one another exclusively through indirect metal–metal contact through an intervening interphase polymeric layer (see the black dotted box denoting one such contact); experimental results for unsintered inks or inks dried in air (please see figure 2) point to such a scenario. (c) Schematic of a self-assembled system of NAgs where the individual NAgs are connected by a mixture of direct metal–metal contact (shown by red dashed box) and indirect metal–metal contact (through the intervening polymeric layer; shown by black dotted box); experimental results for sintered inks (please see figure 2) point to such a scenario. The NAg-polymer-layer composite structure, shown in figure 4, can be considered as a representative NAg that constitutes the NAg assembly shown in part (c).

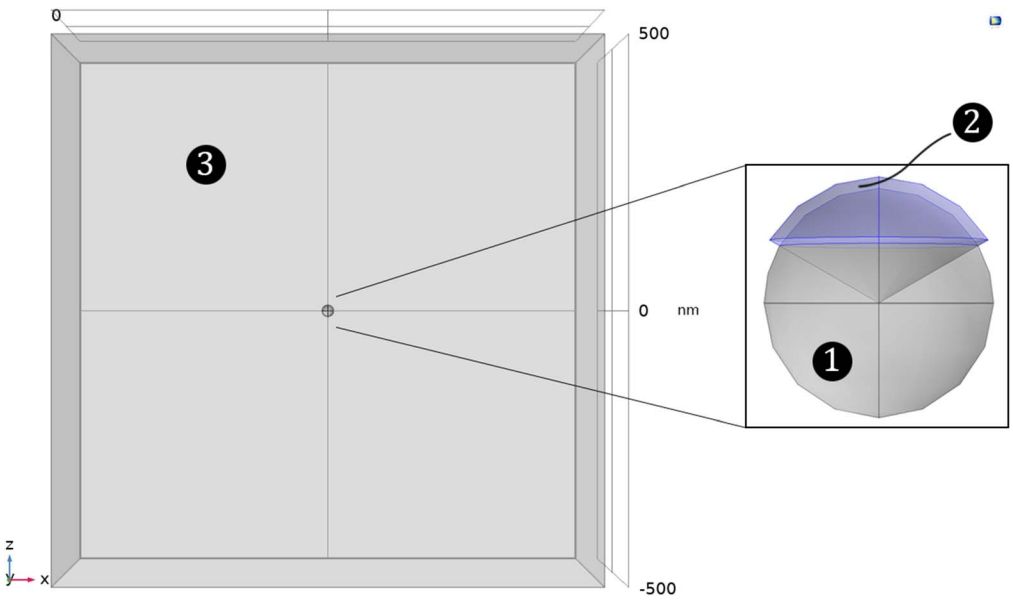

Figure 6. Schematic representation of the simulation domain identifying the three separate zones. The conductivities of region 1, 2, and 3 are considered as σ_m, σ_{int} , and 0.3 σ_m, respectively.

by a partially coated (with a polymeric layer) NAg (shown in figure 4) in a surrounding medium (see figure 6): as explained above, this representation enables the best possible capture of the experimentally observed scenario where the self-assembled NAgs (within the sintered traces) form a mixture of direct metal–metal and indirect metal–metal (through an intervening polymeric layer) contacts. Given that the symmetry condition cannot be applied for the geometry considered in figure 4, we cannot obtain for this case closed-form analytical solutions quantifying the equivalent conductivity, enforcing us to employ a numerical approach (discussed later).

In order to calculate the electric field, Maxwell's equation, which reduces to Poisson's equation (see equation(4)), is solved for each of the three regions of the simulation domain (shown in figure 6):

$$\nabla^2\phi = 0,\ \nabla\phi = -\vec{E}, \tag{4}$$

where ϕ is electrostatic potential.

We subsequently obtain the current density vector $[\vec{J}(\vec{r})]$ by directly multiplying the scalar conductivity field $\sigma(\vec{r})$ (please note the $\sigma(\vec{r})$ accounts for the variation of the conductivity across different regions in the system, as explained above) to the electric field, i.e.

$$\vec{J}(\vec{r}) = \sigma(\vec{r})\vec{E} \tag{5}$$

Obviously, $\sigma(\vec{r})$ appearing in equation (5) is a discontinuous function (or more precisely a piecewise continuous function)

stemming from the fact that the three different regions in our simulation domain (shown in figure 6) have different *constant conductivity values*. However, it is mandatory to enforce the *current continuity* between these different regions in our simulation domain (this *current continuity* condition appears as an interfacial continuity condition): as a result, the electric field naturally becomes discontinuous. This discontinuity in the electric field is a consequence of the charge accumulation at the interface between two materials of unequal conductivities. Under such circumstances, the average current density and the electric field (in z direction) can be expressed as:

$$J_z = \frac{\int_{\text{int}} J_z dV + \int_{\text{np}} J_z dV}{V}, \tag{6}$$

$$E_z = \frac{\int_{\text{int}} E_z dV + \int_{\text{np}} E_z dV}{V}. \tag{7}$$

In equations (6), (7), V is the volume, $\int_{\text{int}} XdV$ and $\int_{\text{np}} XdV$ represent the volume integral of quantity X across the interphase region and the NP region, and J_Z and E_Z represent the vector components of the current density and the electric field in the z direction.

Finally, we can express the equivalent conductivity ($\sigma_{\text{eq},0}$) as:

$$\sigma_{\text{eq},0} = \frac{J_z}{E_z}. \tag{8}$$

It is important that one should also account for the effect of the porosity that exists throughout the system: such a consideration ensures that using equation (2) (with σ_{eq} replacing σ_m), we can get the final value of the equivalent conductivity as

$$\sigma_{\text{eq}} = 0.83\sigma_{\text{eq},0}. \tag{9}$$

Equation (9) suggests that if there was no polymer coating at all, the conductivity of the sintered material would be 83% of the bulk value due to porosity (as is hypothesized in the study of Rosker *et al* [21]).

2.2.4. Numerical procedure. The numerical method (for solving the electric field and the current density) was implemented using the electrostatics module in COMSOL Multiphysics. This module enables the solution for the electric and current density for such composite systems (see figures 4 and 6), which in turn provide the equivalent conductivity.

The geometry (e.g. regions described in figure 6) was achieved in COMSOL using primitives such as cube, sphere and cone, and appropriate Boolean operations. Furthermore, we do a parametric averaging over θ (see figure 4) by rotating our NAg assembly from 0° to 180° in the x–z plane: such a step is necessary as the orientation of the interphase cap in actual sintered inks is randomly positioned with respect to the applied electric field direction.

We keep the prototypical NAg in an otherwise uniform electric field. In COMSOL, we achieve this by creating a bounding box of dimensions hundred times greater than the radius of our NAg, and by assigning constant voltage on top (10 V) and bottom (0 V) faces by using constant Electric Potential boundary condition. However, we note that the actual value of applied voltage has no effect on the value of equivalent conductivity. This is because our differential equations and boundary conditions are linear in applied voltage; hence both current density and electric field scale proportionally with applied voltage to give same ratio of equivalent conductivity. Finally, after attaining the solution for different values of θ, we do the volume averaging of current density and electric field as described in the equations (6)–(8) by using Domain Probes in COMSOL.

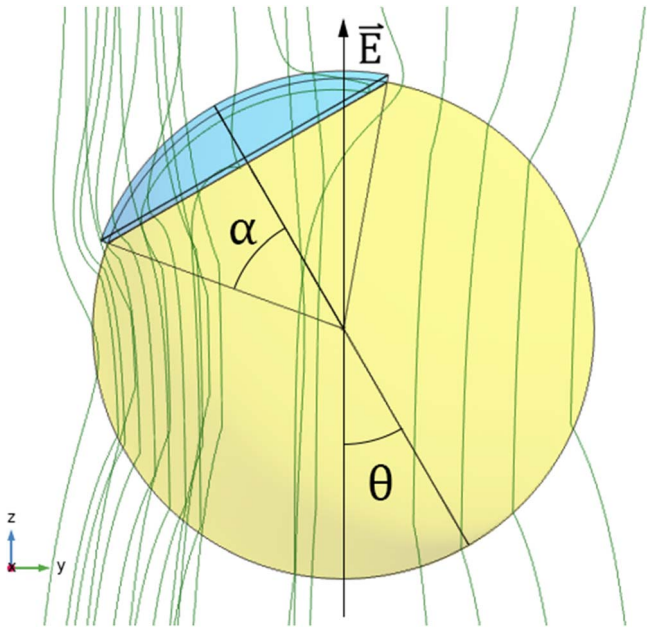

Figure 7. Electric field streamlines (green curves) around the NAg (yellow region is of metal; blue region is of interphase polymer). We consider a representative case where the polymeric layer is characterized by a cone angle of $\alpha = 40°$, which corresponds to 12% of total sphere area covered by the interphase layer (i.e. $\beta = 12\%$). The nanoaggregate is rotated over multiple values of θ to get a statistical average (the picture considers $\theta = 30°$). Additionally, $r_{\text{np}} = 10$ nm (r_{np} is the radius of the NP considered in the simulation) and $t_{\text{int}} = 0.3$ nm.

2.2.5. Simulation results. After doing a mesh convergence study, the average conductivity was calculated for two extreme values of interphase polymeric layer thicknesses (namely $t_{\text{int}} = 0.3$ nm, 1 nm) and two radii of representative NPs or NAgs ($r_{\text{np}} = 10$ nm and 100 nm). The minimum thickness was chosen as 0.3 nm since below a separation distance of 0.3 nm, the silver atoms of two adjacent NPs (or NAgs) will start to interact (due to very large van der Waals forces) fusing the two adjacent NPs. Also, we get a polymer layer thickness of 0.3 nm from the TEM images.

Before discussing the results for the equivalent conductivity, we shall like to discuss the results for the electric field lines in the vicinity of the representative polymer-coated NAg (shown in figure 4). Figure 7 shows the electric field streamlines (green curves) around the NAg in the presence of the applied electric field. If the entire domain had a single conductivity (that of bulk metal), all electric field and current density streamlines would be parallel to the direction of external electric field ($\vec{E}$). However, due to the heterogeneity

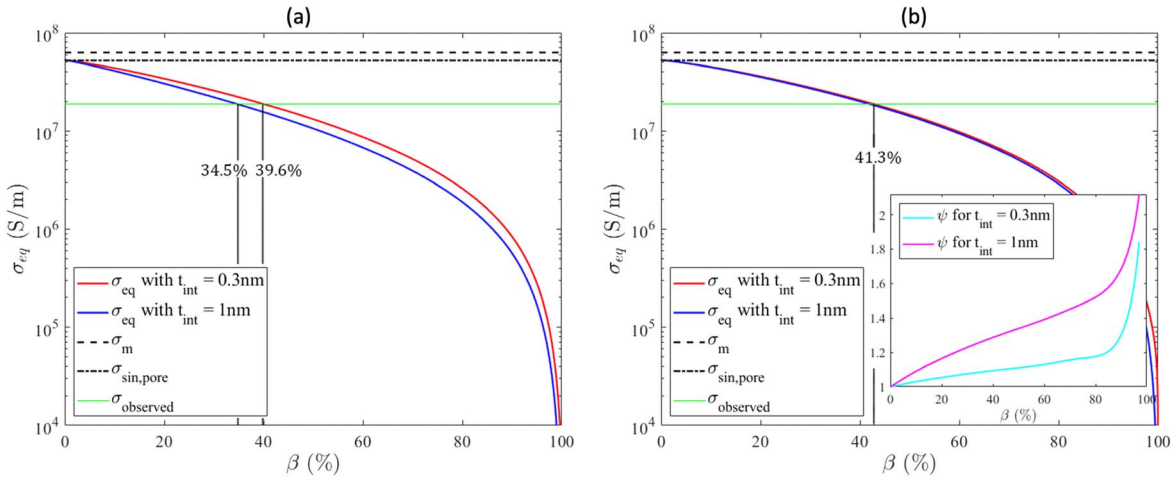

Figure 8. Variation of the simulated values of the equivalent conductivity (σ_{eq}) for different percentages of β (which denotes the fraction of the NP surface covered by the polymeric layer) for different values of the thickness of the polymeric layer (t_{int}) for (a) NAgs (or NPs) of 10 nm dimension and (b) NAgs of 100 nm dimension. In the figure, we also point out the values of bulk metallic conductivity (σ_m), bulk metallic conductivity factoring in the effect of void fraction (considered as 12%) ($\sigma_{sin,pore}$, see equation 1), and the experimentally observed conductivity of the sintered traces ($\sigma_{sin,exp}$ or $\sigma_{observed}$) that is ~30% of σ_m. In both parts (a) and (b), we have identified the value(s) of β corresponding to which σ_{eq} becomes equal to $\sigma_{observed}$. In the inset of part (b), we plot the variation of the conductivity ratio ψ, which is defined as $\psi = \frac{\sigma_{eq} \text{ for NAgsof 100 nm dimension}}{\sigma_{eq} \text{ for NAgs(or NPs) of 10 nm dimension}}$, with percentages of β for different values of the thickness of the polymeric layer (t_{int}).

(stemming from different parts of the NAg-interphase system, namely the metallic part and the polymer coating, having different conductivity values) we see two interesting things. First, when the electric field lines enter the NAg, they get closer to each other, ensuring the prevalence of a larger current density at such locations. Second, due to the presence of the interphase polymeric capping, which is a highly non-conductive region, the field lines get distorted and dispersed while trying to move around the polymer layer. This is the main reason for the drop in conductivity in the NAg-interphase system.

Figure 8 shows the variation of the (numerically computed) equivalent conductivity (σ_{eq}). The curves (shown in figure 8) were obtained for NP (or NAg) dimensions of 10 nm and 100 nm because 10 nm is the smallest possible size of the NP in the ink and 100 nm can appropriately represent the size of the NAgs formed after sintering. In figure 8, β is the ratio of the surface area of the NP covered with interphase material to the total NP surface area. Due to the drastic difference between the conductivities of the NPs and the polymeric material (or in other words, due to the difference between the conductivity associated with the direct metal–metal contact and the conductivity associated with the indirect metal–metal contact through the intervening polymeric layer), the equivalent conductivity dramatically decreases with an increase in β. Figure 8 shows that for $\beta \sim$ 35%–40% (i.e. when 35%–40% of the NP surface is covered by polymeric material), σ_{eq} becomes 30% of the bulk conductivity of the silver (i.e. the scenario typically witnessed for the silver NP traces sintered at 140 °C–150 °C for 15 min [4, 5]). We observe insignificant effect of the thickness of the polymeric layer, for a given NP (or NAg) size, in determining the critical value of β that ensures the attainment of a value of σ_{eq} that is 30% of the bulk conductivity of the silver. On the other hand, the change in the size of the NP (or NAg) seems to have a significant effect on changing the conductivity only for a β value that is much larger than the critical β value (35%–40%) for which the conductivity of the sintered traces becomes ~30% of the bulk conductivity of the silver (see the figure in the inset of figure 8(b)). These observations confirm that the very presence of the polymeric layer and the extent (in terms of β) to which the layer covers the NP (and hence enforces the indirect metal–metal contact through the intervening polymeric layer) is the main factor responsible for reducing the conductivity of the sintered traces.

We shall also like to point out here that we did perform simulations for a set-up that consists of a self-assembled system of NAgs (structure described in figure 5(c)) instead of a single NAg. Such a self-assembled system of NAg might represent a closer analog (than a single NAg) to the experimentally observed configuration within a sintered trace (see figures 2(e)–(g)). The detailed simulation procedure and the simulation results for this self-assembled system of NAgs have been provided in the supporting information (and figures S4 and S5 in the supplementary material). The key finding from these new simulations is that for the case of self-assembled system of NAgs, the critical value of β (i.e. the value of β corresponding to which the conductivity of the sintered traces becomes ~30% of the bulk conductivity) is slightly more than the critical value of β for the case of single NAg (where this critical value of β is 35%–40%, depending on system parameters). For example, for the case where we have considered the self-assembled system of NAgs to consist of twelve NAgs (with the radius of each NAg being 100 nm), the critical value of β becomes ~55%. This difference is rather intuitive: a larger number of NAgs (with each NAg having a conductivity of the bulk metal) contributing to the σ_{eq} will lead to a larger value of σ_{eq}.

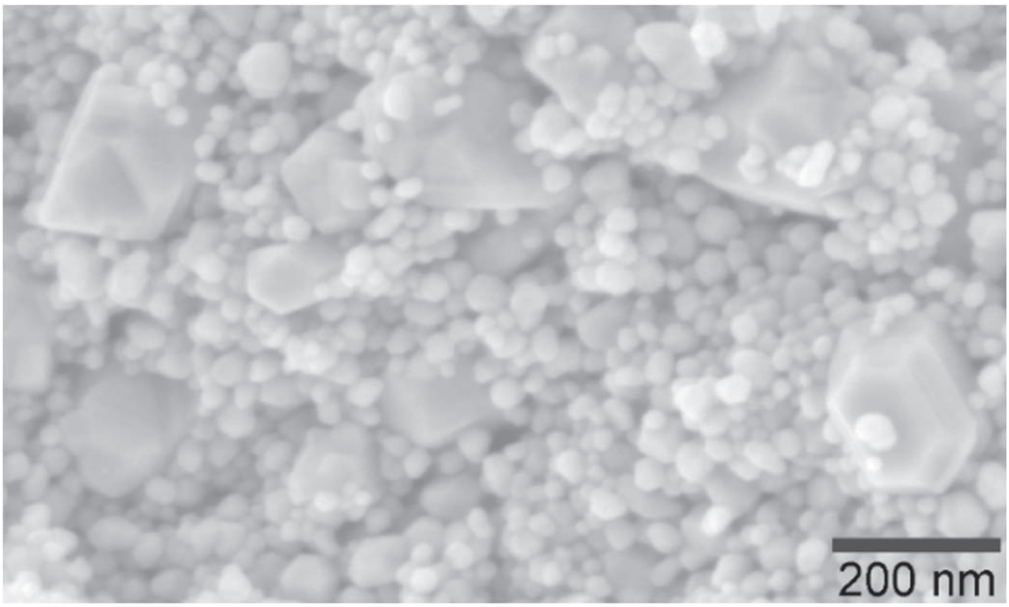

Figure 9. SEM image of the cross-section of a NP ink deposit after sintering at 150 °C.

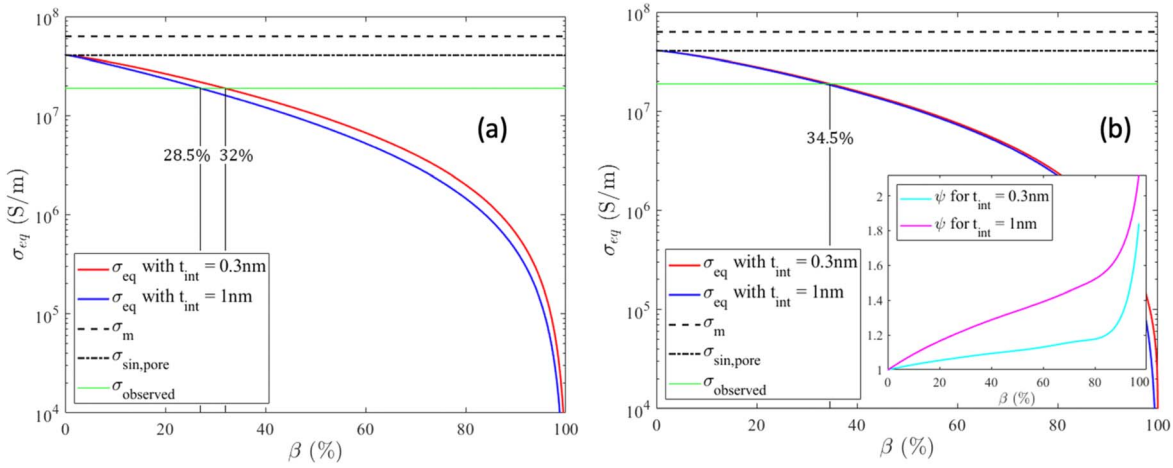

Figure 10. Variation of the simulated values of the equivalent conductivity (σ_{eq}) for different percentages of β (which denotes the fraction of the NP surface covered by the polymeric layer) for different values of the thickness of the polymeric layer (t_{int}) and a 3D porosity of 27% for (a) NAgs (or NPs) of 10 nm dimension and (b) NAgs of 100 nm dimension. In the figure, we also point out the values of bulk metallic conductivity (σ_m), bulk metallic conductivity factoring in the effect of void fraction or porosity (considered as 27%) ($\sigma_{sin,pore}$, see equation 1), and the experimentally observed conductivity of the sintered traces ($\sigma_{sin,exp}$ or $\sigma_{observed}$) that is ~30% of σ_m. In both parts (a) and (b), we have identified the value(s) of β corresponding to which σ_{eq} becomes equal to $\sigma_{observed}$. In the inset of part (b), we plot the variation of the conductivity ratio ψ, which is defined as $\psi = \frac{\sigma_{eq} \text{ for NAgsof 100 nm dimension}}{\sigma_{eq} \text{ for NAgs(or NPs) of 10 nm dimension}}$, with percentages of β for different values of the thickness of the polymeric layer (t_{int}).

Therefore, in order to ensure that $\sigma_{eq} \sim \sigma_{observed}$, a larger coverage by the interphase polymeric material will be needed for the case of self-assembled NAg system.

2.3. Calculations considering 3D porosity of the printed traces

The calculations provided above is based on the TEM-imaging based (see figure 3) porosity values of the 2D NP structure. In real-world printed electronics, however, the printed traces are 'thick' lines that have *3D porosity*. We did print such a line with an undiluted ink and imaged its cross-section with SEM to assess the porosity (see figure 9) after sintering Here a NP trace was printed on aluminum foil, sintered, and then cut with a sharp razor blade to reveal the cross-section for imaging. SEM imaging showed that the nanoparticles were randomly close packed in the sintered deposit with some larger pores on the order of several particle diameters wide (red arrows). It is possible these pores were generated in the creation of the cross-section sample. However, it is not possible to quantify the pore fraction within the deposit based on the SEM image due to the low resolution and 3D nature of the image.

Under such circumstances, we resorted to existing literature to identify the 3D porosity information of the printed traces. There have been some studies that have obtained the 3D porosity of the printed and sintered silver-NP-ink traces indirectly by using density measurements and the values suggest a porosity that is approximately 27% (stemming from a density value of 73% of bulk silver) [32]. In figure 10, we re-plot the variation of the equivalent conductivity with β for this particular porosity value (27%) of the printed and sintered traces. The results indicate a slight decrease in the critical β value (i.e. β value where the equivalent conductivity is equal to the observed conductivity, which is 30% of σ_m) as compared to the case where 2D porosity (12%) was considered (please compare figure 8(a) with figures 10(a) and 8(b) with figure 10(b)).

3. Conclusions

In this paper, we provide an analysis that aims to identify the relative effects of voids and residual polymer layer on NP and NAg surfaces (even after sintering) in the reduced conductivity of sintered traces of metal NP inks. High resolution TEM imaging, providing unprecedented micro-nanoscopic details of the sintered inks, reveal that under typical sintering conditions (e.g. sintering of commercial silver NP inks at 150 °C for 15 min) there exists a significant amount of residual non-conductive polymeric layer on the outer surface of the NAgs present within the sintered traces. The experiments, while confirm the presence of the polymeric surface coverage on the sintered NAgs, it cannot exactly quantify the extent of the coverage of the polymeric layer on the surface of the NAgs. Therefore, we next develop a computational framework, motivated by the experimental finding about the geometry of the sintered NAgs with the presence of polymeric layer on the surface of the NAgs, for calculating the equivalent conductivity of the system that accounts for the specific microstructure of the sintered ink consisting of NAgs and remnant polymeric material: the computations establish that presence of such polymer (to an extent where it covers 35%–40% of the outer surface of the NAgs) can explain the reduced conductivity of the sintered traces. This work therefore highlights the importance of first principles models, informed by the experimental data, to quantify the mechanisms for reduced conductivity in nanoparticle ink deposits. We anticipate that this finding will motivate the vast research community that works with metal NP based conductive inks to design such inks that employ less amount of polymeric material, or employ polymeric materials that are either completely removed at ~150 °C (possibly by a mechanism such as chemical sintering) or are more conductive (e.g. conductive polymers): such design improvement will ensure enhanced conductivity of the sintered traces without necessitating an increase in the sintering temperature or the time of sintering.

4. Materials and methods

4.1. TEM and EDS

Samples for TEM were prepared by drop casting 1 μl of silver NP ink (Novacentrix, Metalon JS-A101A) diluted either 1000 (for PSD analysis) or 10 times (for porosity and sintering studies) by volume with DI water onto lacey carbon coated copper TEM sample grids (01894, Ted Pella, USA), following by drying in atmosphere at room temperature. After initial imaging of the NP deposit, the entire sample was baked in an oven at 150 °C for 15 min TEM imaging, STEM imaging, and EDS were performed in a JEOL JEM-2100F with a Schottky emitter operating at 200 kV. STEM and TEM images were processed in ImageJ and EDS data were processed in the Bruker EDS software. EDS elemental analysis was performed by collecting and integrating the characteristic x-ray peaks of each element (Ag, C, O) as a function of position along a line scanned across the NP surface using a Bruker Flash 6T/60 windowless silicon EDS detector. Porosity and particle size measurements from TEM images were performed using custom image analysis algorithms coded in house in MATLAB.

4.2. Scanning electron microscopy

Ink deposits were prepared by printing silver NP ink (Novacentrix, Metalon JS-A101A) on aluminum foil. The ink was deposited in short lines ~10 cm long on aluminum foil. Ink was deposited in several passes to build up a deposit that was 10–15 μm thick after printing and curing at 150 °C. A razor blade was used to cut through the deposits and reveal the cross-section. The sample was mounted using an aluminum sample stub with the cross-section surface normal to the electron beam. The cross-section was imaged with a scanning electron microscope (SEM) (Hitachi SU70) using 5 kV beam energy and an Everhardt-Thornley secondary electron detector.

4.3. Dynamic light scattering

DLS was performed on a photon correlation spectrometer (Photocor instruments, Estonia, EU). The NP ink sample was diluted 18 000 times by volume with DI water. The detector was situated at an angle of 90° to the laser pathway. The autocorrelation function was fit to a multi-exponential decay function and the hydrodynamic diameter distribution was extracted from fits of the autocorrelation function using the Stokes-Einstein equation assuming spherical particles.

4.4. Thermogravimetric analysis

Thermogravimetric analysis (TGA) was performed on a Shimadzu TGA-50. A milligram quantity of ink was added to the alumina crucible and the temperature was increased initially to 100 °C for 10 min to evaporate the residual solvent. Then the temperature was increased up to 400 °C with a heating rate of 10 °C min^{-1} in air.

4.5. Supporting information

Additional results for sintering conducted at 300 °C; Results for thermogravimetric analysis and ink printing; Derivation of the Relationship of 2D pore fraction to 3D pore fraction; simulation results and discussions for the system consisting of self-assembled NAgs instead of a single NAg.

Acknowledgments

This material is based upon work supported by, or in part by, the National Center for Manufacturing Sciences (under agreement 202096) and the US DEVCOM Army Research Laboratory under other transaction agreement number W911NF-20-90011. The authors acknowledge Kyle Ludwig for assistance with thermogravimetric analysis experiments.

Data availability statement

All data that support the findings of this study are included within the article (and any supplementary files).

ORCID iDs

Siddhartha Das https://orcid.org/0000-0002-1705-721X

References

[1] Wu W 2017 Inorganic nanomaterials for printed electronics: a review *Nanoscale* **9** 7342–72
[2] Nayak L, Mohanty S, Nayak S and Ramadoss A 2019 A review on inkjet printing of nanoparticle inks for flexible electronics *J. Mater. Chem.* C **7** 8771–95
[3] Kamyshny A and Magdassi S 2019 Conductive nanomaterials for 2D and 3D printed flexible electronics *Chem. Soc. Rev.* **48** 1712–40
[4] Ding J, Liu J, Tian Q, Wu Z, Yao W, Dai Z, Liu L and Wu W 2016 Preparing of highly conductive patterns on flexible substrates by screen printing of silver nanoparticles with different size distribution *Nanoscale Res. Lett.* **11** 412
[5] Mo L *et al* 2019 Nano-silver ink of high conductivity and low sintering temperature for paper electronics *Nanoscale Res. Lett.* **14** 197
[6] Magdassi S, Grouchko M, Berezin O and Kamyshny A 2010 Triggering the sintering of silver nanoparticles at room temperature *ACS Nano* **4** 1943–8
[7] Tang Y, He W, Zhou G, Wang S, Yang X, Tao Z and Zhou J 2012 A new approach causing the patterns fabricated by silver nanoparticles to be conductive without sintering *Nanotechnology* **23** 355304
[8] Dalal N, Gu Y, Chen G, Hines D, Dasgupta A and Das S 2019 Effect of gas flow rates on quality of aerosol jet printed traces with nanoparticle conducting ink *J. Electron. Packag.* **142** 011012
[9] Liu S, Yuen M and Kramer-Bottiglio R 2019 Reconfigurable electronic devices enabled by laser-sintered liquid metal nanoparticles *Flexible Printed Electron.* **4** 015004
[10] McKenzie J and Desai S 2018 Investigating sintering mechanisms for additive manufacturing of conductive traces *Am. J. Eng. Appl. Sci.* **11** 652–62
[11] Deore B *et al* 2019 Formulation of Screen-Printable Cu molecular ink for conductive/flexible/solderable Cu traces *ACS Appl. Mater. Interfaces* **11** 38880–94
[12] Shou W, Mahajan B, Ludwig B, Yu X, Staggs J, Huang X and Pan H 2017 Low-cost manufacturing of bioresorbable conductors by evaporation–condensation-mediated laser printing and sintering of zn nanoparticles *Adv. Mater. (Weinheim, Ger.)* **29** 1700172
[13] Tan H W, Saengchairat N, Goh G L, An J, Chua C K and Tran T 2020 Nduction sintering of silver nanoparticle inks on polyimide substrates *Adv. Mater. Technol.* **5** 1900897
[14] Wang Z, Wang W, Jiang Z and Yu D 2016 Low temperature sintering nano-silver conductive ink printed on cotton fabric as printed electronics *Prog. Org. Coat.* **101** 604–11
[15] Fu Q, Stein M, Li W, Zheng J and Kruis F E 2020 Conductive films prepared from inks based on copper nanoparticles synthesized by transferred arc discharge *Nanotechnology* **31** 025302
[16] Lee D, Kim D, Moon Y and Moon S 2013 Effect of laser-induced temperature field on the characteristics of laser-sintered silver nanoparticle ink *Nanotechnology* **24** 265702
[17] Park J, Kang H, Shin K and Kang H 2016 Fast sintering of silver nanoparticle and flake layers by infrared module assistance in large area roll-to-roll gravure printing system *Sci. Rep.* **6** 34470
[18] Rahman M, Cheng C, Karagoz B, Renn M, Schrandt M, Gellman A and Panat R 2019 High performance flexible temperature sensors via nanoparticle printing *ACS Appl. Nano Mater.* **2** 3280–91
[19] Hummelgård M, Zhang R, Nilsson H and Olin H 2011 Electrical sintering of silver nanoparticle ink studied by in-situ tem probing *PLoS One* **6** e17209
[20] Zhang X, Liu W, Li H, Xia S, Tsung C, Liu H, Liu W and Yu Y 2021 *In situ* probing the kinetics of gold nanoparticle thermal sintering in liquids: implications for ink-jet printing *ACS Appl. Nano Mater.* **4** 2538–46
[21] Rosker E, Barako M, Nguyen E, DiMarzio D, Kisslinger K, Duan D, Sandhu R, Goorsky M and Tice J 2020 Approaching the practical conductivity limits of aerosol jet printed silver *ACS Appl. Mater. Interfaces* **12** 29684–91
[22] Meng F and Huang J 2019 Evolution mechanism of photonically sintered nano-silver conductive patterns *Nanomaterials* **9** 258
[23] Wünscher S, Rasp T, Grouchko M, Kamyshny A, Paulus R M, Perelaer J, Kraft T, Magdassi S and Schubert U S 2014 Simulation and prediction of the thermal sintering behavior for a silver nanoparticle ink based on experimental input *J. Mater. Chem.* C **2** 6342–52
[24] Trindade G F *et al* 2021 Roberts. residual polymer stabiliser causes anisotropic electrical conductivity during inkjet printing of metal nanoparticles *Comm. Mater.* **2** 47
[25] Dissanayake T U, Wang M and Woehl T J 2021 Revealing reactions between the electron beam and nanoparticle capping ligands with correlative fluorescence and liquid-phase electron microscopy *ACS Appl. Mater. Interfaces* **13** 37553–63
[26] Du Y K, Zang P, Mou N G, Hua N P and Jiang L 2006 Thermal decomposition behaviors of pvp coated on platinum nanoparticles *J. Appl. Polymer Sci.* **99** 23–6
[27] Lee J, Nakouzi E, Song M, Wang B, Chen J and Li D 2018 Mechanistic understanding of the growth kinetics and dynamics of nanoparticle superlattices by coupling interparticle forces from real-time measurements *ACS Nano* **12** 12778–87
[28] Pal G and Kumar S 2016 Multiscale modeling of effective electrical conductivity of short carbon fiber-carbon nanotube-polymer matrix hybrid composites *Mater. Des.* **89** 129–36

[29] Wang G, Wang C, Tang C, Zhang F, Sun T and Yu X 2018 Two-Stage electrical percolation of metal nanoparticle–polymer nanocomposites *J. Phys. Chem.* C **122** 8614–20

[30] Feng C and Jiang L 2013 Micromechanics modeling of the electrical conductivity of carbon nanotube (cnt)–polymer nanocomposites *Compos.* A **47** 143–9

[31] Simmons J 1963 Generalized formula for the electric tunnel effect between similar electrodes separated by a thin insulating film *J. Appl. Phys.* **34** 1793–803

[32] Bourassa J, Ramm A, Feng J Q and Renn M J 2019 Water vapor-assisted sintering of silver nanoparticle inks for printed electronics *SN Appl. Sci.* **1** 517